

Conference Proceedings Paper

Functional nano-hydroxyapatite for applications in conservation of stony monuments of cultural heritage

Francesco Capitelli ¹, Bujar Dida ², Giancarlo Della Ventura ³, Francesco Baldassarre ⁴, Davide Capelli ¹, Giorgio S. Senesi ⁵, Altin Mele ⁶, Dritan Siliqi ⁴

¹ Istituto di Cristallografia, IC-CNR, Via Salaria Km 29.300, 00016 Monterotondo (Rome), Italy; francesco.capitelli@ic.cnr.it (F.C.); davide.capelli@ic.cnr.it (D.C.)

² FIMIF, University Polytechnic of Tirana, Tirana, Albania; bujar.dida@fimif.edu.al (B.D.)

³ Dipartimento di Scienze, Università Roma Tre, Largo S. L. Murialdo 1, Rome, 00146, Italy; giancarlo.dellaventura@uniroma3.it (G.D.V.)

⁴ Istituto di Cristallografia, IC-CNR, Via G. Amendola, 122/O, 70126 Bari, Italy; francesco.baldassarre@ic.cnr.it (F.B.); dritan.siliqi@ic.cnr.it (D.S.)

⁵ Istituto per la Scienza e Tecnologia dei Plasmi, ISTP-CNR, Via G. Amendola, 122/O, 70126 Bari, Italy; giorgio.senesi@cnr.it (G.S.S.)

⁶ Ivodent Academy, Center of Techniques Studies, Tirana, Albania; altin.mele@ivodent.edu.al (A.M.)

* Correspondence: francesco.capitelli@ic.cnr.it; Tel.: +39-06-90672616.

Published: 6 November 2020

Abstract: Stony monuments have high artistic value and need continuously to be preserved from the damages of time, in particular from the detrimental effects of the weathering. One of the new environmentally-friendly (nano) materials for stone consolidation, particularly suitable for marble and calcareous (limestone, sandstone) artifacts, is $\text{Ca}_{10}(\text{PO}_4)_6(\text{OH})_2$ hydroxyapatite (HAp), which shows a considerably lower dissolution rate and solubility compared to CaCO_3 calcite, the building block of marble materials, especially in acidic environments, thus having been proposed for the protection of calcareous monuments against acidic rain corrosion. Promising results were obtained, but further optimization is necessary as the treated layer is often incomplete, cracked and/or porous. Many parameters have to be optimized to obtain a coherent and homogenous layer, and consequently to avoid the formation of metastable, soluble phases instead of HAp: the role of the pH of the starting solution; the effect of organic and inorganic additions, and in particular that of ethanol, that is reported to adsorb on calcite, hence possibly favoring the growth of the HAp layer. The formation of HAp nanoparticles and the applications on stony substrates were investigated by means of a multi-methodological approach, based on scanning electron microscopy, x-ray diffraction, small- and/or wide-angle x-ray scattering, Fourier-transform Infrared spectroscopy, completed by in situ measurements of laser-induced breakdown spectroscopy and acid attack preliminary test on stony substrates.

Keywords: Hydroxyapatite; nanoparticles; synthesis; structural characterization; stony monuments; laser-induced breakdown spectroscopy

Introduction

Rocks are among the most durable construction materials used in historic buildings all over the world. However, over time, the stone can be subject to various degradation processes leading to physical and chemical modifications. Although these effects may be limited to the surface and negligible to the structural stability of the affected buildings, they can represent a major problem in decorative elements of artistic value, where any detail should be preserved [Pesce et al., 2019]. The challenge for conservators and material scientists involved in stone conservation has always been to find a way to stop or delay the effects of these degradation

processes. The basic principle of the patrimony is that the cultural heritage is an incalculable and integral legacy to our future: observing and knowing the past, will help next generations to better challenge the future. Thus, conservation of stone heritage is always a delicate and complex task, due to the multiple variables that have to be taken into account to identify the problems, and to define the necessary conservation actions and to select materials and best procedures to be used. The variety of factors to be analyzed includes the intrinsic stone properties (from geological features up to mechanical behavior), the state of conservation, the degradation mechanisms and the environmental factors.

One of the most promising technology employed for lowering the previously described degradation processes, is that of nanomaterials, nowadays largely applied in the maintenance of the world cultural heritage, with the aim of improving the consolidation and protection treatments of damaged stone materials they are made of [David et al., 2020]. Such nanomaterials display important advantages that could solve many problems found in the traditional interventions, that often show the serious bias of the lack the vital compatibility with the original substrate and a durable performance. Application of nanotechnology in the cultural heritage conservation is characterized by the possibility to design consolidant products strongly compatible with the original stone substrate. Moreover, when particles have dimensions of about 100 nanometers, the material properties change significantly from those at larger scales. The nanoparticles must show: stability and sustained photoactivity; biological and chemical inactivity, nontoxicity, as well as antimicrobial properties for lowering ecotoxicological impact on animals and plants [Reyes-Estebanez et al., 2018]; low cost suitability towards visible or near UV light, high conversion efficiency and high quantum yield. In addition, these treatments should also possess water repellent properties which favor the self-cleaning action and prevent the generation of damage caused by water. The most commonly used inorganic consolidant agents are the products based on $\text{Ca}(\text{OH})_2$ calcium hydroxide nanoparticles [El Bakkari et al., 2019], due to their compatibility with a large part of the built and sculptural heritage. As well as other hydroxides ($\text{Mg}(\text{OH})_2$, $\text{Sr}(\text{OH})_2$), metal oxides (TiO_2 , ZnO), and metal nanoparticles (Au, Ag, Pt) have been reported in the literature, focusing on their potential as consolidants on different artifacts of cultural heritage [David et al., 2020, Dida et al., 2020]. But one of the most challenging nanomaterial is $\text{Ca}_{10}(\text{PO}_4)_6(\text{OH})_2$ hydroxyapatite (HAP), already applied in a large variety of technological and biomedical applications, mainly due to its close relationship with mineral component of hard human tissues [Rakovan & Pasteris, 2015; Baldassarre et al., 2020], and in cultural heritage conservation used for carbonate stone consolidation [David et al., 2020]. HAP can be applied for the consolidation of limestones, marbles and sandstones with different carbonate contents. This product is not introduced directly into stone material, if not only locally, but as an aqueous solution of diammonium hydrogen phosphate (DAP) with calcium ions coming from the CaCO_3 calcite mineral, the main constituents of marbles and limestone (of carbonate substrates), which can derive from the partial dissolution of the same substrate. Thanks to its low viscous nature, this aqueous consolidant product is able to penetrate deeply into the stone, generating a significant improvement in mechanical properties of the same stone. The HAP has been tested as a protective treatment for marble against acid rain corrosion [Graziani et al., 2016]. The study of compatibility and adaptability requires that the physical and chemical properties of both consolidator products and stone substrate are well known. Such a knowledge plays a very important role for the good outcome of the present project. Materials of interest, synthesized in our labs has been analyzed by using: 1) X-ray diffraction (XRD), effective on crystalline materials and able to carry out information on chemical composition, size, shape and atomic structure, 2) small- and/or wide-angle scattering (SAXS/WAXS), powerful tool to investigate the domain of phosphate particles as a function of their optical properties; in the case of SAXS the technique can be applied to HAP nanoparticles characterization; 3) Fourier-Transform Infrared (FTIR) spectroscopy, reliable techniques for investigating hydroxyl anions and variations within anionic and cationic groups in the obtained materials; 4) scanning electron microscopy for checking morphologies of nanoparticles; 5) biological evaluation of the antimicrobial properties of obtained HAP materials, through direct contact and disc diffusion methods versus most common gram + and gram - bacteria present in human or animal biosystems 6) Laser-induced breakdown spectroscopy (LIBS), a micro-destructive technique able to get quali-quantitative information on museums artifacts.

Experimental

Synthesis. Hydroxyapatite powder was prepared by chemical-precipitation method at 25 °C and pH = 10. All chemicals used were purchased from Sigma-Aldrich St Louis, Missouri, USA, with purity higher than 99%. A mixture of $\text{Ca}(\text{NO}_3)_2 \cdot 4\text{H}_2\text{O}$ (MW = 236 g/mol), and $(\text{NH}_4)_2\text{HPO}_4$ (MW = 132 g/mol) was employed as starting material; ultrapure water (conductivity of 0.055 $\mu\text{S}/\text{cm}$ at 25 °C) was used; $(\text{NH}_4)_2\text{HPO}_4$ was dissolved to obtain 37 ml of solution 0.6 mol/l (0.0222 moles of P) into a three-neck round-bottomed flask made of Pyrex, and stirred at 400 rpm; meanwhile the pH of phosphorous-containing solution was adjusted at 10.00 with an aqueous solution of NaOH (2 mol/l) and stirred. A solution of 50 ml of $\text{Ca}(\text{NO}_3)_2$ was added drop by drop at 2.5 ml/min by peristaltic-pump and stirred constantly with pH measured and adjusted at 10.00 ± 0.05 in order to minimize the formation of secondary phases and to prevent the aggregation of the particles during their formation [Baldassarre et al., 2020]; after 20 min of reaction and precipitation, the solution was aged at 25 °C for 24h and calcinated at 900 °C according to the following reaction [Jarcho et al., 1976]:



The precipitates were centrifuged at 10000 rpm for 5 minutes, washed and centrifuged five times with deionized water with 5% v.v⁻¹ of ethanol using liquid-liquid ratio equal to 1.

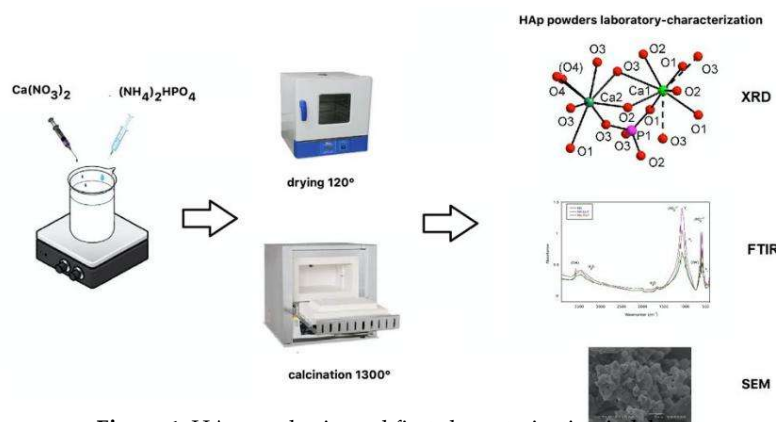


Figure 1. HAp synthesis, and first characterization in laboratory.

X-ray diffraction (XRD) is typically employed to investigate the changes of crystalline phases in samples. Powder XRD data were collected at room temperature by using an automated Rigaku RINT2500 diffractometer (50 KV, 200 mA) equipped with the silicon strip Rigaku D/teX Ultra detector. An asymmetric Johansson Ge (111) crystal was used to select the monochromatic Cu $K\alpha_1$ radiation ($\lambda = 1.54056 \text{ \AA}$). The main acquisition parameters are reported in Table 2. The angular range 8–100° (2θ) was scanned with a step size of 0.02° (2θ) and counting time of 4 s/step. Measurements were executed in transmission mode by introducing the sample within a glass capillary with a 0.3 mm of internal diameter and mounted on the axis of the goniometer. A capillary spinner was used during measurements to reduce effects of preferred orientation of crystallites. The determination of the unit cell parameters and the space group were carried out by EXPO2013 software [Altomare et al., 2013].

Small angle X-ray scattering (SAXS) is the most used technique to determine the morphology features of a set of nanoparticles. The technique takes advantage of the electron density function difference between the studied objects and surrounding medium. Small-angle X-ray scattering (SAXS) is a technique where the elastic scattering of X-rays by a sample is recorded at very low angles (typically 0.1–10 measured from the beam axes). This angular range contains information regarding the structure of scatterer entities, like nanoparticles and micro- and macromolecules, among others. Depending of the studied systems, SAXS technique could provide information of the distances between partially ordered materials, pore sizes, as well as other data [Glatter and Kratky, 1982], depending on

the experimental setup, SAXS is capable of delivering structural information of objects whose size ranges between 0.5 and 100 nm.

Wide angle X-ray scattering (WAXS) is the technique that is most identified with molecular structure at the resolution of atomic positions and is sometimes used synonymously with x-ray diffraction. The term x-ray diffraction conventionally describes the discrete scattering associated with crystalline samples, either in a single oriented crystal or a powder composed of small, randomly oriented crystals packed together. The important distinction between SAXS and WAXS is that the WAXS measures the x-rays scattered into angles large enough to define probe lengths that are comparable to atom-atom spacings and atomic planes in a crystal. Because the intensity of the scattered x-rays is measured at higher angles, the collimation and flight path requirements are more compact for a dedicated WAXS instrument relative to instruments optimized for SAXS. A higher level of morphological and structural information can be gained by collecting SAXS and WAXS data, individually or in combination (SWAXS) [Altamura et al., 2012].

Fourier transform infrared (FTIR) spectroscopy is one of the techniques most widely used for molecular characterization. Powder FTIR spectra were collected on a Nicolet iS50 FTIR spectrometer equipped with a DTGS detector and a KBr beam splitter; nominal resolution was 4 cm⁻¹ and 64 scans were averaged for both sample and background. The HAp sample was prepared as KBr disks, by mixing 1 mg of sample with 200 mg of KBr.

Scanning Electron Microscopy (SEM) electron microscopy observations were done by a high-resolution FE-SEM Zeiss Gemini at LIME (*Laboratorio Interdipartimentale di Microscopia Elettronica*), University Roma Tre. The instrument is equipped with two SE (secondary electrons), one 5-sectors BSE (back scattered electrons) and a CL (cathodo-luminescence) detectors, besides a high-resolution EDS 60mm² detector for elemental analysis.

Biological evaluation of the antimicrobial properties of obtained HAp materials, through direct contact and disc diffusion methods versus most common Gram + and Gram - bacteria present in animal or plant biosystems. These two techniques allow the observation of the antimicrobial activities of the Hap sample. Briefly, in the direct contact method a bacterial suspension is transferred to a vial containing the material and then the mixture is spread onto agar plates and incubated for several hours. After this period, the number of bacterial colonies on each plate is counted and compared against growth-positive control in absence of materials [Resmin et al., 2019]. The disc diffusion test is performed on an agar plate containing sterilized filter paper discs, which have been previously treated and soaked with Hap nanoparticles. Upon the spread onto the plate of the bacterial suspension and a period of incubation, the diameters (mm) of the inhibition zone can be measured and compared with both positive and negative controls [Phatai et al., 2019].

Laser-induced breakdown spectroscopy (LIBS) is a versatile technique that provides nearly instant multi-elemental analysis including low atomic number elements e.g. Be, C, Li, F, Na, Mg, Al, and Si of materials, both in the laboratory and in the field. This is achieved by focusing a short laser pulse on the surface of the sample, and by analyzing the resulting spectrum from the laser-induced plasma. LIBS has been employed in the analysis of archaeological sites, historical monuments and ancient artifacts for assessing the qualitative, semi-quantitative and quantitative elemental content of materials such as pigments, pottery, glass, stones, metals, minerals, meteorites, gems and fossils [Senesi, 2014; Anglos, 2019]. A simple scheme of a working LIBS set-up is depicted in Fig. 2.

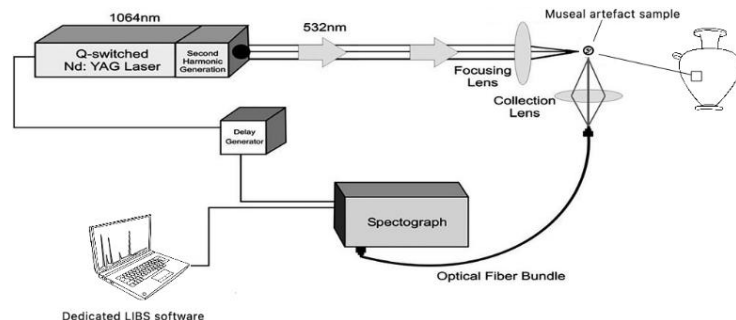


Figure 2. Typical LIBS set-up.

3. Characterization

3.1. X-ray qualitative study

For HAp compound under investigation, the indexation of the powder diffraction pattern was obtained through EXPO2013 software [Altomare et al., 2013]. Crystallinity = 81% was achieved according to [Landi et al., 2000]. Unit cell parameters, $a=b=9.4145(4)$ Å, $c=6.8758(5)$ Å, $V=6.8758(5)$ Å³, are similar to those of most common HAp phases [Wilson et al., 1999; Rossi et al., 2011], while the space group determination gave the most common hexagonal $P6_3/m$ space group of apatite [Wilson et al., 1999; Rossi et al., 2011]. In the powder pattern of HAp, some unindexed peaks were detected and assigned to $\text{Ca}_3(\text{PO}_4)_2$ (TCP) phase [Yashima et al., 2003]; quantitative phase analysis carried out by EXPO2013 gave HAp 88.9% and TCP 11.1% in the sample. This result is in agreement with the finding of [Kong et al., 2002; Skorokhod et al., 2010] who report partial dissociation of HAp into TCP at about 900°C, and with previous investigations on TCP [El Khouri et al., 2017; Capitelli et al., 2018; Altomare et al., 2019]. Fig. 3 reports a typical XRD spectrum for HAp calcined at 900°, together with most important reflections.

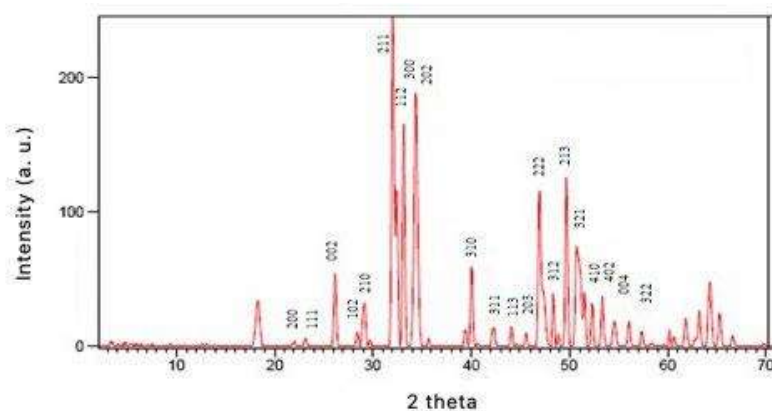


Figure 3. Typical XRD spectrum of HAp calcined at 900°.

3.2. X-ray crystal structure

Structural sites of HAp are those known for hexagonal $P6_3/m$ HAp, with Ca atoms engaged in complex coordination: according to usual notations for site apatite site labelling [Rossi et al., 2011], Ca1 is involved in a CaO_6 metaprism (a solid figure intermediate between an octahedron and trigonal prism (Figure 4a), while Ca2 shows a $\text{CaO}_6(\text{OH})$ geometry (Fig. 4b), resembling a distorted CaO_7 pentagonal bipyramid with an equatorial plane occupied by O1 and two couples of symmetry-related O3 atoms and, vertices occupied by O2 atom and OH group (corresponding to O4 atom) [Baldassarre et al., 2020]. Worthy of note is the wide range of cationic substitutions within HAp structure, from Mn, Na, Fe, Zn for different biomedical applications [Badassarre et al., 2020], up to rare earth elements for luminescent imaging applications [Baldassarre et al., 2020, Paterlini et al., 2020].

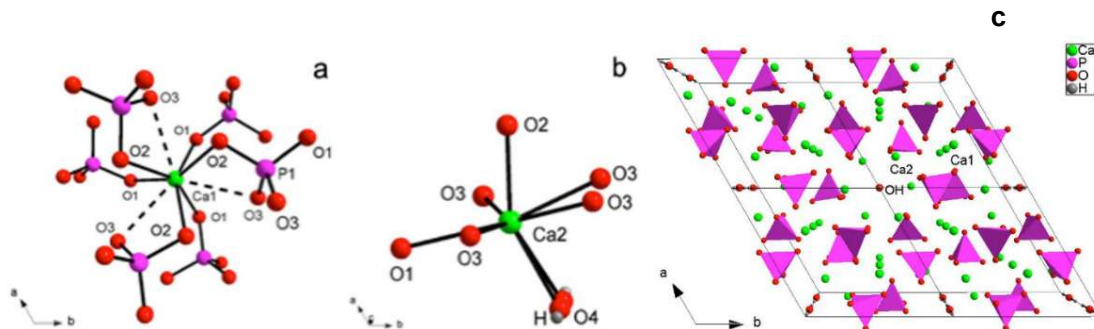


Figure 4. Ca1 (a) and Ca2 (b) coordination environments in HAp. Representation, down crystallographic axis c , of the three-dimensional framework of HAp (c). Dashed lines: Ca-O interactions with bonding character.

To describe the hexagonal $P6_3/m$ HAp structure, we can better write the crystal formula as $[\text{Ca}(1)_4\text{Ca}(2)_6](\text{PO}_4)_6(\text{OH})_2$, which underlines the two cationic site; a close inspection, indeed, suggests that HAp shows a zeolitic character where the framework consists of columns of face-sharing Ca_1O_6 metaprisms corner-connected to six different PO_4 tetrahedra down $[001]$ making up $[\text{Ca}(1)_4(\text{PO}_4)_6]_{10-}$ anionic moieties; this network results in one-dimensional hexagonal tunnels occupied by $[\text{Ca}(2)_6(\text{OH})_2]_{10+}$ counter-ions (Figs. 4c). The strong $\text{Ca}1 \dots \text{O}3$ interactions (Fig. 4a) further stabilizes the structure (Fig. 4c) [Baldassarre et al., 2020].

3.3. SEM microscopy

High-resolution SEM investigation of HAp samples show the presence of different morphologies, such as compact and porous aggregates, and massive assemblages. The porous aggregates are the most common, with the largest crystallite size of $\sim 10 \mu\text{m}$ (Figs. 1a, 1c). The massive fragments and compact aggregates have the largest dimension $\sim 35 \mu\text{m}$ (Figs. 1c, 1e and 1f) and $\sim 5 \mu\text{m}$ (Fig. 1e), respectively. In all cases, the crystallites show a rounded morphology, from elongated to sub-spherical, and the most common dimension is $\sim 5 \mu\text{m}$. SEM investigations also suggested the growth of porous morphologies on massive fragments (Figs. 1d, 1f).

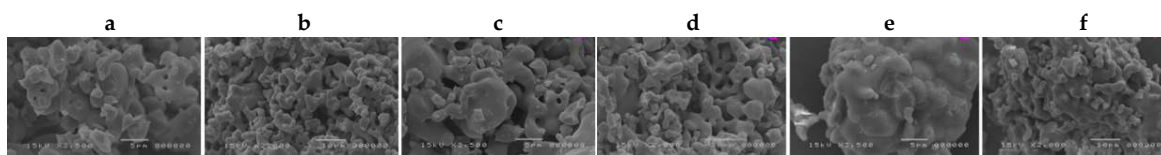


Figure 5. SEM images of synthetic HAP samples with different morphologies.

3.4. FTIR Spectroscopy

The literature on the interpretation of the FTIR spectra of hydroxyapatite is quite exhaustive [Koutsopoulos et al., 2002; Jastrzębski et al., 2011; El Khouri et al., 2019], being it a well-established technique but at the same time particularly useful while able to detect with accuracy (OH) groups in HAp (Baldassarre et al., 2020; Paterlini et al., 2020). Phosphorous compounds typically show a strong molecular character with respect to their vibrational properties, therefore FTIR spectra are dominated by internal $(\text{PO}_4)^{3-}$ modes. The spectrum of HAp, shows an intense doublet at $1091\text{--}1039\text{ cm}^{-1}$ assigned to the asymmetric stretching (ν_3) while the weak peak at 962 cm^{-1} can be assigned to the symmetric stretching mode of the $[\text{PO}_4]^{3-}$ group [El Khouri et al., 2019]. Two medium intense and very sharp peaks at 602 and 564 cm^{-1} can be related to the triple degenerate antisymmetric bending mode of the $[\text{PO}_4]^{3-}$ group [Iconaru et al., 2013]. The sharpness of such bands, according to [Markovic et al., 2004], is a reliable indicator of a well-crystallized HAp, in agreement with the result of crystallinity from XRD data. Worthy of note, the spectrum of HAp shows a well-resolved sharp peak at 3570 cm^{-1} , due to the stretching mode of the (OH)- group [Koutsopoulos et al., 2002]. This peak is superimposed to a broad absorption due to H_2O (moisture) adsorbed on the KBr disk [Predoi et al., 2007]; the bending mode of this moisture is also visible as a broad component at 1600 cm^{-1} . Analysis of deuterated samples [Fowler, 1974] shows that the relatively sharp peak at 663 cm^{-1} is due to the O-H libration (as reported in inset in Fig. 6). In Fig. 6 a FTIR spectrum of a synthetic HAp is reported, while Table 1 reports measured absorption in the FTIR spectrum and relative assignments for HAp sample.

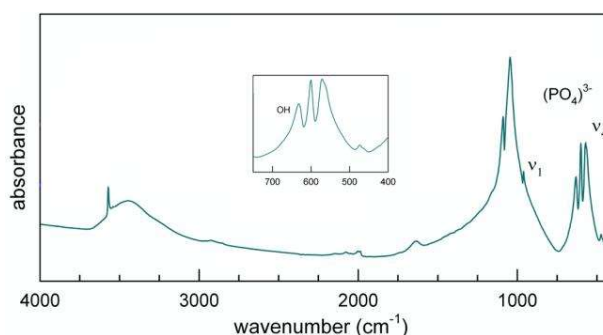


Figure 6. FTIR spectrum of calcined HAp (900).

HAp	Assignment
3571	$\nu_s(\text{OH})$
1637	$\delta(\text{H}_2\text{O})$
1089	
1046	$\nu_3(\text{PO}_4)^{3-}$
962	$\nu_1(\text{PO}_4)^{3-}$
632	$\delta(\text{OH})$
601	
570	$\nu_4(\text{PO}_4)^{3-}$
473	$\nu_2(\text{PO}_4)^{3-}$

Table 1. Measured absorption in the FTIR spectrum and relative assignments for HAp sample.

3.5. SAXS/WAXS

SAXS can be used to study the morphological properties of Hap nanoparticles and in this way to follow the crystallization process and the role and influence of various experimental setup parameters (temperature, speed, time etc) and/or additives to accelerate/inhibit the process. In this way it would be possible to control the size and shape of the Hap nanoparticles. Once SAXS experimental curves have been obtained, software such as SasView (www.sasview.org) can be used to estimate/refine the shape and average size of the particles, as well as their polydispersity [Degli Esposti et al., 2020].

3.6. Biological evaluation of the antimicrobial properties of obtained nanophases.

As with all surface treatments, Hap nanoparticles can be leached into the surrounding environment leading to potential ecotoxicity in soil and water, with adverse effects on the associated biota and the bacteria-dependent processes [Reyes-Estebanez et al., 2018]. Even though there is limited understanding of the environmental fate of engineered nanoparticles after release from treated surfaces, ecotoxicological studies reported different results of bacterial inhibition, stimulation, survival and death, which depend on dose, species and test procedures [Eduok et al., 2017].

HAp nanoparticles may enter the soil and water systems pertinent the archeological sites directly, by leaching from building surfaces, or indirectly, via wastewater sludges used as fertilizers. Nano HAp tend to partition into the sludge in wastewater treatment plants and their disposal into soil can result in contamination by the particles themselves, or their transformation products [Reyes-Estebanez et al., 2018]. For this reason, a careful interest is devoted on the topic of biological evaluation of the HAp nanophases, although the need of a standard test for antimicrobial efficacy to determine their impact on ecological processes still exists.

The anti-microbial activity and properties of HAp nanoparticles can be assessed *in vitro* by direct contact and disc diffusion methods in a solid medium, using common Gram + and Gram - bacteria abundant in animal and plant biosystems. Anyway, a variety of methods of determining antimicrobial activity have been previously studied, showing that the results obtained are profoundly influenced by the method selected, microorganism used to carry out the test and the degree of solubility of each test compound [Valgas et al., 2007].

3.7. LIBS

In the last decades, LIBS has been widely applied to cultural heritage. Nowadays, the use of handheld (h) LIBS instrumentation is considered a future prospective for this field. Senesi et al. (2018) were one of the first study to apply hLIBS in archeological geological applications. A limestone fragment was analyzed from a masonry block at the Castello Svevo in Bari (Italy) that exhibited surface degradation in the form of a black crust. Both the unaltered limestone core and the surface alteration crust were analyzed at ten different

positions. The single, averaged LIBS spectrum provided the sample's geochemical fingerprint based on eight elements - C, Na, Mg, Al, Si, Ca, Fe, and K. As expected, C, Mg and Ca were the major constituents of the unaltered limestone (Fig. 7), whereas the altered surface layer was characterized by the presence of Al, Si, and Fe plus lesser amounts of Na and K derived from the marine aerosol.

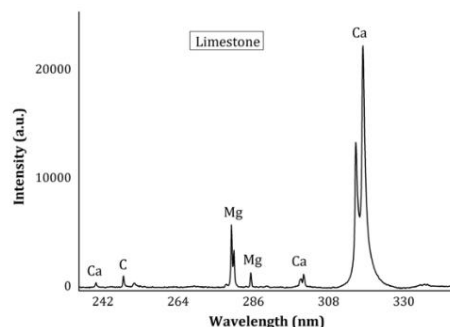


Figure 7. LIBS spectrum acquired in the range 240-335 nm showing the C line at 247.85 nm, Ca lines at 239.86, 300.68, 300.94, 315.88, 317.93 nm and Mg lines at 285.21, 279.55, 280.27 nm in the unaltered limestone sample.

3.8. Carbonatic substrate treatment

HAp coating is usually formed by mixing aqueous solutions at various concentrations of DAP with CaCl₂ calcium chloride and making them react with calcitic powders. CaCl₂ is added to different formulations, so that the Ca²⁺ ions necessary for the reaction can be provided without dissolution of the carbonate substrate. (CaCl₂:DAP = 1:1000). The (0.1 M DAP + 0.1 mM CaCl₂) solution resulted to be of the most promising [Graziani et al., 2016]. The concentration was chosen on the basis of preliminary experiments to avoid an excessive thickness of the treated layer that would lead to drying cracks, and the solution was modified to study the influence of pH, cationic additions, ethanol additions, etc [Graziani et al., 2016].

3.9. Acid attack preliminary test.

The main mechanism that leads to carbonate surface recession is the dissolution in CO₂ saturated water at pH 5.6, while the contribution of acid rain attack is lower, being the pH range of rain substantially between pH 4 and pH 5.5; for this reason, no significant variations are expected by lowering the pH inside that range, while a further decrease would result in switching to a more acidic regime, controlled by different kinetics. Moreover, HAp is known to be the most stable calcium phosphate in a pH range spanning from 4 to 4.5. For this reason, in case soluble phases were formed from the reaction, the behavior of samples at very low pH (below 4) would not be representative of their behavior at pH > 4 [Graziani et al., 2016].

The optimization of HAp treatment for carbonate surfaces protection toward acid rain was investigated [Graziani et al., 2016], highlighting that samples treated at pH 11, despite the initial assumption that the higher amount of (PO₄)₃⁻ that form as a result of DAP dissociation would enhance HAp growth, are less acid resistant. This is probably due to higher layer porosity and to the formation of soluble phases together with HAp. Moreover, the fast deprotonation of (HPO₄)₂⁻ makes the practical advantage negligible. None of the tested cationic additions at pH 11 allowed for a better efficacy of the treatments. Besides, the addition of ethanol in very low concentration remarkably increases the resistance of HAp treated samples and the uniformity of the treated layer, thus making it possible to reduce the concentration of diammonium hydrogen phosphate (DAP) used and control the thickness of the treated layer.

References

- Altamura, D.; Lassandro, R.; Vittoria, F.A.; De Caro, L.; Siliqi, D.; Ladisa, M.; Giannini, C.. "X-ray microimaging laboratory (XMI-LAB)." *J. Appl. Crystallogr.* **2012**, *45*, 869–873.
- Altomare, A.; Cuocci, C.; Giacobbo, C.; Moliterni, A.; Rizzi, R.; Corriero, N.; Falcicchio, A. *EXPO2013*: a kit of tools for phasing crystal structures from powder data. *J. Appl. Crystallogr.* **2013**, *46*, 1231–1235.
- Altomare, A.; Rizzi, R.; Rossi, M.; El Khouri, A.; Elaamrani, M.; Paterlini, V.; Della Ventura, G.; Capitelli, F. New $\text{Ca}_{2.90}(\text{Me}_{2+})_{0.10}(\text{PO}_4)_2$ β -tricalcium Phosphates with $\text{Me}_{2+} = \text{Mn, Ni, Cu}$: Synthesis, Crystal-Chemistry, and Luminescence Properties. *Crystals* **2019**, *9*, 288.
- Baldassarre F., Altomare A., Corriero N., Mesto E., Lacalamita M., Bruno G., Sacchetti A., Dida B., Karaj D., Della Ventura G.D., Capitelli, F., Siliqi, D. Crystal Chemistry and Luminescence Properties of Eu-Doped Polycrystalline Hydroxyapatite Synthesized by Chemical Precipitation at Room Temperature. *Crystals* **2020**, *10*, 250.
- Capitelli, F.; Rossi, M.; El Khouri, A.; Elaamrani, M.; Corriero, N.; Sodo, A.; Della Ventura, G. Synthesis, structural model and vibrational spectroscopy of lutetium tricalcium phosphate $\text{Ca}_9\text{Lu}(\text{PO}_4)_7$. *J. Rare Earth*. **2018**, *36*, 1162–1168.
- David, M.E., Ion, R.-M., Grigorescu, R.M., Iancu, L., Andrei, E.R. Nanomaterials Used in Conservation and Restoration of Cultural Heritage: An Up-to-Date Overview. *Materials* **2020**, *13*, 2064.
- Degli Esposti, L.; Adamiano, A.; Tampieri, A.; Ramirez-Rodriguez, G.B.; Siliqi, D.; Giannini, C.; Ivachenko, P.; Martra, G.; Lin, F.H.; Delgado-Lopez, J.M.; Lafisco, M. Combined Effect of Citrate and Fluoride Ions on Hydroxyapatite Nanoparticles. *Cryst. Growth Des.* **2020**, *20*, 3163–3172
- Dida B., Siliqi D., Baldassarre, F., Karaj D., Hasimi A., Kasemi V., Nika V., Vozga I. "Nanomaterialialet për Konservimin e Trashëgimisë Kulturore", SHLBSH, Tirana (2020), ISBN 978-99943-2-468-2.
- Eduok S., Coulon F. Engineered nanoparticles in the environments: interactions with microbial systems and microbial activity. In: *Microbial ecotoxicology*, Cham. Cravo-Laureau et al. editors. Springer: Cham **2017** pag. 63 - 107.
- El Bakkari M, Bindiganavile V, Boluk Y. Facile Synthesis of Calcium Hydroxide Nanoparticles onto TEMPO-Oxidized Cellulose Nanofibers for Heritage Conservation. *ACS Omega* **2019**, *4*, 20606–20611.
- El Khouri, A.; Elaamrani, M.; Della Ventura, G.; Sodo, A.; Rizzi, R.; Rossi, M.; Capitelli, F. Synthesis, structure refinement and vibrational spectroscopy of new rare-earth tricalcium phosphates $\text{Ca}_9\text{RE}(\text{PO}_4)_7$ (RE = La, Pr, Nd, Eu, Gd, Dy, Tm, Yb). *Ceram. Int.* **2017**, *43*, 15645–15653.
- El Khouri, A.; Zegzouti, A.; Elaamrani, M.; Capitelli, F. Bismuth-substituted hydroxyapatite ceramics synthesis: Morphological, structural, vibrational and dielectric properties. *Inorg. Chem. Comm.* **2019**, *110*, 107568.

1 Fowler, B.O. Infrared studies of apatites. I. Vibrational assignments for calcium, strontium, and barium
2 hydroxyapatites utilizing isotopic substitution. *Inorg Chem.* **1974**, *13*, 194–207.
3
4 Graziani G., Sassoni E., Franzoni E., Scherer G.W. Hydroxyapatite Coatings for Marble Protection:
5 Optimization of Calcite Covering and Acid Resistance. *Appl. Surf. Sci.* **2016**, *368*, 241-257.
6
7 Glatter, O., & Kratky, O. (1982). Small-angle X-ray scattering. London: Academic.
8
9 Iconaru, S.-L.; Motelica-Heino, M.; Predoi, D. Study on Europium-Doped Hydroxyapatite Nanoparticles
10 by Fourier Transform Infrared Spectroscopy and Their Antimicrobial Properties. *J. Spectrosc.* **2013**, *2013*,
11 1–10.
12
13 Jarcho, M.; Bolen, C.H.; Thomas, M.B.; Bobick, J.; Kay, J.F.; Doremus, R.H. Hydroxylapatite synthesis and
14 characterization in dense polycrystalline form. *J. Mater. Sci.* **1976**, *11*, 2027–2035.
15
16 Jastrzębski, W.; Sitarz, M.; Rokita, M.; Bułat, K. Infrared spectroscopy of different phosphates structures.
17 *Spectrochim. Acta A* **2011**, *79*, 722–727.
18
19 Kong, L.B.; Ma, J.; Boey, F. Nanosized hydroxyapatite powders derived from coprecipitation process. *J.*
20 *Mater. Sci.* **2002**, *37*, 1131–1134.
21
22 Koutsopoulos, S. Synthesis and characterization of hydroxyapatite crystals: A review study on the
23 analytical methods. *J. Biomed. Mater. Res.* **2002**, *62*, 600–612.
24
25 Landi, E.; Tampieri, A.; Celotti, G.; Sprio, S. Densification behaviour and mechanisms of synthetic
26 hydroxyapatites. *J. Eur. Ceram. Soc.* **2000**, *20*, 2377–2387.
27
28 Markovic, M.; Fowler, B.O.; Tung, M.S. Preparation and comprehensive characterization of a calcium
29 hydroxyapatite reference material. *J. Res. Natl. Inst. Stand. Technol.* **2004**, *109*, 553.
30
31 Paterlini, V.; Bettinelli, M.; Rizzi, R.; El Khouri, A.; Rossi, M.; Della Ventura, G.; Capitelli, F.
32 Characterization and Luminescence of Eu³⁺- and Gd³⁺-Doped Hydroxyapatite Ca₁₀(PO₄)₆(OH)₂. *Crystals*
33 **2020**, *10*, 806.
34
35 Pesce C., Moretto L.M., Orsega E.F., Pesce G.L., Corradi M., Weber J. Effectiveness and Compatibility of a
36 Novel Sustainable Method for Stone Consolidation Based on Di-Ammonium Phosphate and Calcium-
37 Based Nanomaterials. *Materials* **2019**, *12*, 3025.
38
39 Phatai P., Futralan C.M., Kamonwannasit S., Khemthong P. Structural characterization and antibacterial
40 activity of hydroxyapatite synthesized via sol-gel method using glutinous rice as a template. *J. Sol-Gel.*
41 *Sci. Techn.* **2019**, *89*, 764–775.
42
43 Predoi, D.; Barsan, M.; Andronescu, E.; Vatasescu-Baltan, R.A.; Costache, M. Hydroxyapatite-iron oxide
44 bioceramic prepared using nano-size powders. *J. Optoelectron. A. Mat.* **2007**, 3609–3613.
45
46 Rakovan J.R., Pasteris J.D. A technological gem: Materials, Medical, and Environmental Mineralogy of
47 Apatite. *Elements* **2015**, *11*, 195-200.
48
49 Reyes-Estebanez, M., Ortega-Morales, B.O., Chan-Bacab, M., Granados-Echegoyen, C., Camacho-Chab,
50 J.C., Pereanez-Sacarias J.E., Gaylarde C. Antimicrobial engineered nanoparticles in the built cultural
51 heritage context and their ecotoxicological impact on animals and plants: a brief review. *Heritage Science*
52 **2018**, *6*, 52.
53
54 Resmin C.M., Dalpasquale M., Vielmo N.I.C., Mariani F.Q., Villalba J.C., Anaissi F.J., Caetano M.M., Tusi
55 M.M. Study of physico-chemical properties and in vitro antimicrobial activity of hydroxyapatites
56 obtained from bone calcination. *Progress in Biomaterials* **2019**, 8:1-9.
57
58 Rossi, M.; Ghiara, M.R.; Chita, G.; Capitelli, F. Crystal-chemical and structural characterization of
59 fluorapatites in ejecta from Somma-Vesuvius volcanic complex. *Am. Mineral.* **2011**, *96*, 1828–1837.
60

61 Senesi, G.S.; Capitelli, F. Compositional, mineralogical and structural investigation of meteorites by XRD
62 and LIBS. in *Hypersonic Meteoroid Entry Physics*. Eds Colonna et al. IOP series in Plasma Physics. **2019** doi:
63 10.1088/2053-2563/aae894ch5.
64
65 Senesi, G.S. Laser-Induced Breakdown Spectroscopy (LIBS) applied to terrestrial and extraterrestrial
66 analogue geomaterials with emphasis to minerals and rocks. *Earth-Sci. Rev.* **2014**, *139*, 231-267.
67
68 Senesi, G.S.; Manzini, D.; De Pascale, O. Application of a laser-induced breakdown spectroscopy
69 handheld instrument to the diagnostic analysis of stone monuments. *Appl. Geochem.* **2018**, *96*, 87-91.
70
71 Skorokhod, V.V.; Solonin, S.M.; Dubok, V.A.; Kolomiets, L.L.; Permyakova, T.V.; Shinkaruk, A.V. Solonin,
72 S.M.; Dubok, V.A.; Kolomiets, L.L.; Permyakova, T.V.; Shinkaruk, A.V.. Decomposition activation of
73 hydroxyapatite in contact with β -tricalcium phosphate. *Powder Metall. Met. C+* **2010**, 5–6.
74
75 Valgas C., Machado de Souza S., Smânia E.F.A., Smânia Jr A. Screening methods to determine
76 antibacterial activity of natural products. *Braz. J. Microb.* **2007**, *38*, 369-380
77
78 Wilson, R.M.; Elliott, J.C.; Dowker, S.E.P. Rietveld refinement of the crystallographic structure of human
79 dental enamel apatites. *Am. Mineral.* **1999**, *84*, 1406–1414.
80
81 Yashima, M.; Sakai, A.; Kamiyama, T.; Hoshikawa, A. Crystal structure analysis of β -tricalcium
82 phosphate $\text{Ca}_3(\text{PO}_4)_2$ by neutron powder diffraction. *J. Sol. State Chem.* **2003**, *175*, 272–277.
83
84
85
86



© 2020 by the authors. Submitted for possible open access publication under the terms and conditions of the Creative Commons Attribution (CC BY) license (<http://creativecommons.org/licenses/by/4.0/>).

87